Volume 14
Number 10
12 March 2026
Pages 3773–4174

Journal of Materials Chemistry C

Materials for optical, magnetic and electronic devices

rsc.li/materials-c

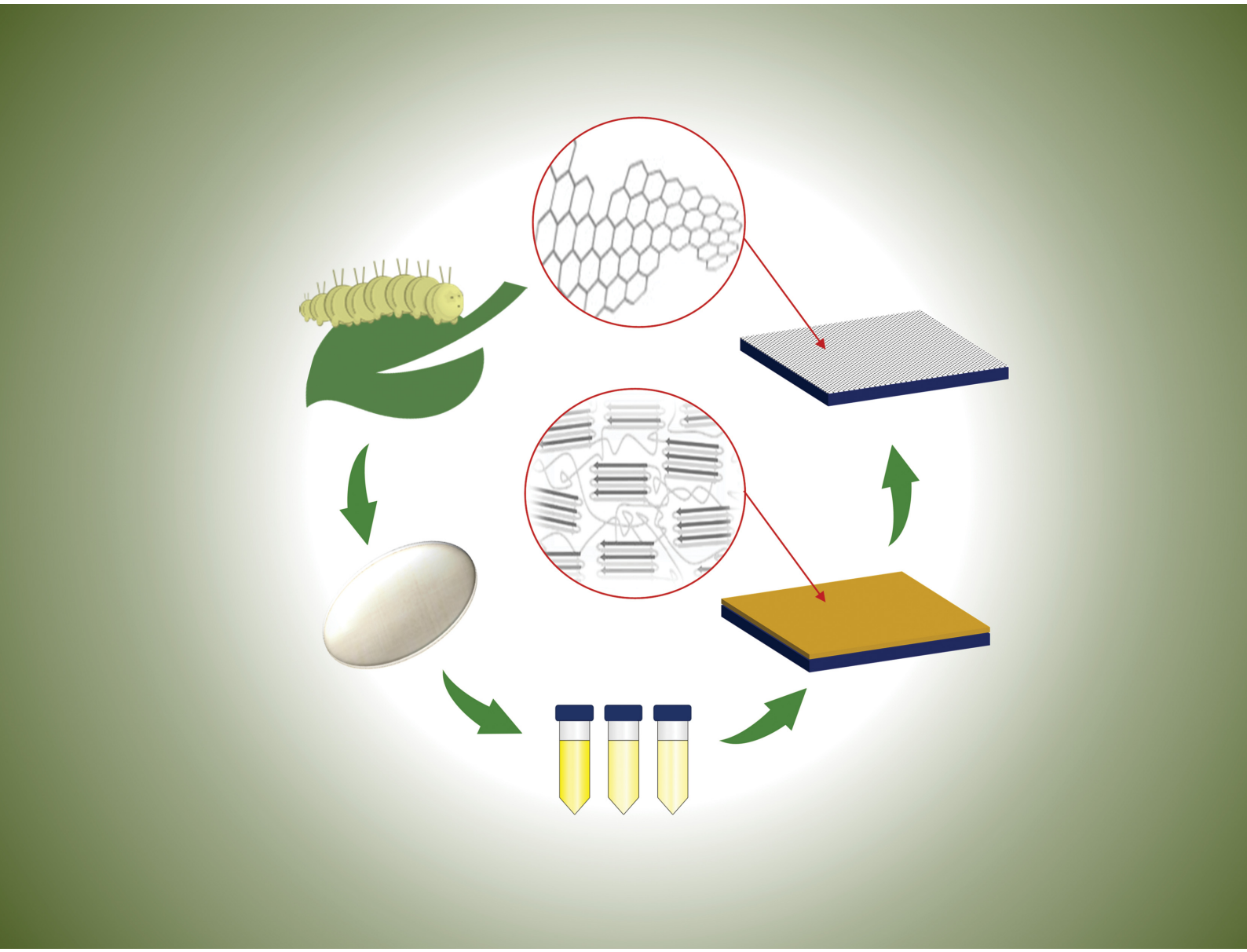

ISSN 2050-7526

ROYAL SOCIETY OF CHEMISTRY

PAPER

Mostafa Bedewy *et al.*

Silk-derived carbon nanosheets for transparent conducting electrodes on flexible substrates

Journal of Materials Chemistry C

ROYAL SOCIETY OF CHEMISTRY

PAPER

View Article Online
View Journal | View Issue

Cite this: J. Mater. Chem. C, 2026, 14, 3890

Silk-derived carbon nanosheets for transparent conducting electrodes on flexible substrates

Se Youn Cho,[ab] Moataz Abdulhafez,[a] Golnaz Najaf Tomaraei,[a] Jaegeun Lee [ac] and Mostafa Bedewy *[ade]

Received 3rd November 2025,
Accepted 25th December 2025

DOI: 10.1039/d5tc03917g

rsc.li/materials-c

Transparent conducting films (TCFs) were fabricated through the transformation of silk fibroin (SF), a renewable natural biopolymer, into carbon nanosheets (CNSs) *via* a catalyst free carbonization process. By adjusting the SF concentration, spin coating rate, and heat treatment temperature, the thickness of the CNS films was tuned from 3.7 to 38.8 nm, while maintaining uniform and smooth surfaces with R_a values between 0.28 and 0.62 nm. Structural analyses showed that pseudo-graphitic nanodomains gradually developed as the heat treatment temperature increased, and these changes directly influenced the optical and electrical properties. The optimized CNS films exhibited an optical transmittance of up to 95.7% at 550 nm and an electrical conductivity of 4.4×10^2 S cm^{-1}, achieving a balanced combination of transparency and conductivity comparable to other solution-processed carbon electrodes. This study provides a scalable and sustainable method for producing ultrathin and flexible carbon-based TCFs and offers clear guidance on the relationships among processing conditions, structural features, and the resulting material properties using silk fibroin as a renewable precursor.

Introduction

Transparent conducting films (TCFs) exhibiting high optical transmittance and electrical conductivity are essential components in modern optoelectronic devices including displays, solar cells, transistors, and sensors.[1–9] In particular, with the growing demand for portable and wearable electronics, flexible TCFs have attracted tremendous attention from both academia and industry. Conventional TCFs are typically manufactured by depositing conductive materials onto transparent substrates. Among these, indium tin oxide (ITO) remains the dominant commercial option due to its excellent optical and electrical properties, including a sheet resistance of 20 Ω/□ and a transmittance of up to 80%.[10] However, the application of ITO in flexible and bendable devices is limited due to its brittle nature with a low crack onset strain of around 1% and high resistance at low annealing temperature as well as its high-cost.[11,12] These limitations have motivated the exploration of alternative materials that can combine flexibility, transparency, and conductivity.

A variety of materials have been investigated as ITO replacements, including metal nanowire networks, conducting polymers, carbon nanotube (CNT) films, and graphene.[1,7,13–19] Among them, metal nanowire and CNT networks have been extensively studied materials for the flexible TCFs. However, their commercial applications are still suffering from the high cost, surface roughness, and poor interfacial adhesion to polymeric substrates. Graphene films, composed of hexagonally arranged sp^2-bonded carbon atoms, have been suggested as a promising alternative due to their exceptional electrical, mechanical, and optical properties.[17,20] However, although solution-based chemical exfoliation allows large scale production of graphene, it inevitably introduces oxygen containing functional groups and structural defects that degrade electrical performance unless additional chemical reduction steps are used.[21,22] In addition, chemical vapor deposition can yield high-quality graphene over large areas, but the necessary metal etching and transfer steps often introduce cracks and pinholes that increase the sheet resistance of the transferred films.[23]

Recently, solution-processed carbon nanosheet (CNS)-based TCFs derived from polymeric precursors such as polyacrylonitrile, pitch, polydopamine, and polyimide has been explored.[17,18] Simple thermal conversion of organic precursors enables the fabrication of few-nanometer-thick CNS films with excellent electrical and optical properties, offering a low-cost and scalable route to nanocarbon-based electrodes.[24–26]

[a] Department of Industrial Engineering, University of Pittsburgh, Pittsburgh, Pennsylvania, 15261, USA. E-mail: mbedewy@pitt.edu
[b] RAMP Convergence Research Center, Korea Institute of Science and Technology, 92 Chudong-ro, Bongdong-eup, Wanju-gun, Jeonbuk, 55324, Republic of Korea
[c] School of Chemical Engineering, Pusan National University, Busan, 46241, Republic of Korea
[d] Department of Mechanical Engineering and Materials Science, University of Pittsburgh, Pittsburgh, Pennsylvania, 15261, USA
[e] Department of Chemical and Petroleum Engineering, University of Pittsburgh, Pittsburgh, Pennsylvania, 15261, USA

Nevertheless, most synthetic polymer precursors are derived from petroleum-based feedstocks and require harsh or toxic solvents, which raises concerns regarding sustainability and environmental impact.

Silk fibroin (SF) produced by *Bombyx mori* (*B. mori*, domestic silkworm) is a protein-based natural polymer, which has been used for high quality clothing since ancient times.[27] Recently, SF has gained significant attention for biomedical applications owing to its biocompatibility, biodegradability, and mechanical robustness.[28] In addition, SF has emerged as a promising class of bio-renewable carbon precursor owing to its natural abundance and relatively high carbon yield. Diverse formats and morphologies of the as-synthesized nanocarbon materials such as plates, spheres, and nanosheets can be easily fabricated in an eco-friendly using regenerated SF solution.[29–31] The carbon microstructure can be regulated by controlling not only the pyrolysis process but also β-sheet crystal structure (geometrically sheet-like 2D motifs) which can transform into polyhexagon structure by thermal heating.[31,32]

In this work, we report a catalyst-free and solution-based method for fabricating ultrathin silk-derived CNS films as flexible transparent electrodes. Regenerated SF was spin-coated into precursor films with precisely tunable thickness, followed by methanol-induced crystallization and high-temperature pyrolysis (800–1200 °C). By systematically examining the effects of SF concentration, spin-coating rate, and heat-treatment temperature (HTT), we elucidate how these parameters govern film thickness, surface roughness, chemical transformation, and electrical properties. The resulting CNS films display sub-nanometer roughness, uniform morphology, remarkable optical transparency, and well-developed pseudo-graphitic ordering that collectively yield high-performance TCFs. This study establishes a sustainable and scalable route for producing ultrathin silk-derived CNS electrodes and reveals the fundamental processing–structure–property relationships governing their optoelectronic performance.

Experimental

Preparation of regenerated silk fibroin solution

Cocoons of *B. mori* silkworm were purchased from the Uljin Farm, South Korea. Regenerated SF solution was prepared following a previously reported method.[33,34] Briefly, the cocoons were soaked in an aqueous solution of 0.02 M sodium carbonate (Na_2CO_3, >99.0%, Sigma-Aldrich Co., USA) and boiled for 30 min. After washing thoroughly with deionized (DI) water to remove the glue-like sericin proteins and other impurities, the extracted fibrous materials (SF) were dried on a clean-bench at room temperature for 3 days. The SF was dissolved in a 9.3 M lithium bromide (LiBr > 99.0%, Sigma-Aldrich Co., USA) solution at 60 °C for 6 hours and then dialyzed in DI water using a Slide-a-Lyzer dialysis cassette (MWCO 3500, Pierce, USA) for 4 days. The final concentration of the SF in the aqueous solution was estimated to be approximately 7 wt%. The solution was kept in the refrigerator (~4 °C) before use.

Preparation of SF thin films

The regenerated SF solution was diluted into the desired concentration ranging from 0.5 to 4 wt% by adding DI water with slow stirring at 4 °C. The SF solutions were spin-coated onto 2 × 2 cm SiO_2/Si wafer substrates (University Wafer Company, Boston, MA, thickness of SiO_2 layer is about 300 nm) with four different spin rates (1000, 3000, 5000, and 7000 rpm). About 100 μL of the solution was used for each experiment and the spin cast time was 45 seconds. After soft baking at 100 °C for 5 min, the SF thin films were immersed in a mixture of methanol, ethanol, and water in the ratio of 9 : 1 : 1 for 12 hours in order to induce β-sheet crystal structure.[35]

Preparation of SF-derived CNSs

A tube-type furnace was used for the carbonization of the samples. The spin-coated SF samples were heated to 150 °C, followed by a dwell time of 30 min in order to remove absorbed water molecules. After isothermal pyrolysis for 3 h at 350 °C, the samples were heated to the desired HTT (800, 1000, and 1200 °C). All the pyrolysis processes were conducted in a nitrogen atmosphere at a rate of 5 °C min^{-1} (Fig. S1).

Characterizations

The thickness of the SF thin film on a SiO_2/Si substrate was measured by an Alfa-step IQ surface profiler (KLA Tencor) and atomic force microscopy (AFM) equipped with a NanoScope V controller. The surface morphologies of SF thin films and SF-based CNSs were examined using AFM. X-ray photoelectron spectroscopy (XPS, PHI 5700 ESCA, Physical Electronics Inc., USA) was used with monochromatic Al-Kα radiation ($h\nu$ = 1486.6 eV) in order to examine the type of chemical bond of carbon and the chemical composition of samples. Raman spectroscopy was carried out using a continuous-wave linearly polarized laser (wavelength: 514.5 nm; 2.41 eV; power: 16 mW). The morphology of the SF-derived carbon was observed using field-emission transmission electron microscopy (FE-TEM, JEM2100F, JEOL, Tokyo, Japan). After transferring onto PET film, the transmittances of the SF-derived CNS films were measured using an Agilent 8453 UV-visible spectrophotometer (Agilent Technologies, Germany).

Results and discussion

Thickness and morphological control of spin-cast silk fibroin films

SF-derived CNSs were prepared from regenerated SF solution through a facile spin-casting process followed by controlled pyrolysis at temperatures up to 1200 °C. TCFs were subsequently fabricated by transferring the SF-derived CNSs onto flexible and optically transparent polyethylene terephthalate (PET) substrates as schematically illustrated in Fig. 1. To obtain uniform SF thin films prior to carbonization, aqueous SF solutions with concentrations of 0.5, 1.0, and 2.0 wt% were spin-coated onto SiO_2/Si substrates at rotational speeds of 1000, 3000, 5000, and 7000 rpm. Film thicknesses were quantified by

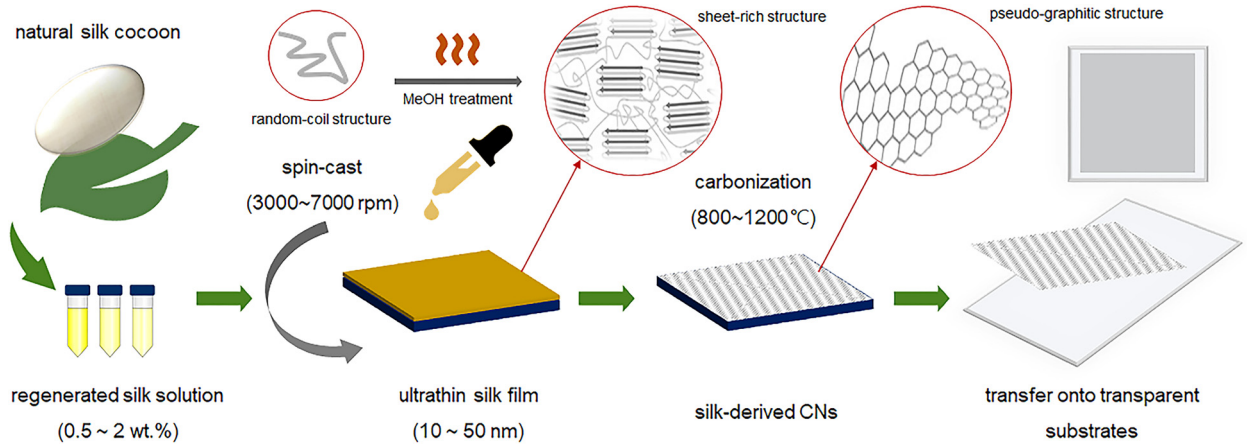

Fig. 1 Schematic illustration of synthesis of silk fibroin-based transparent conducting film.

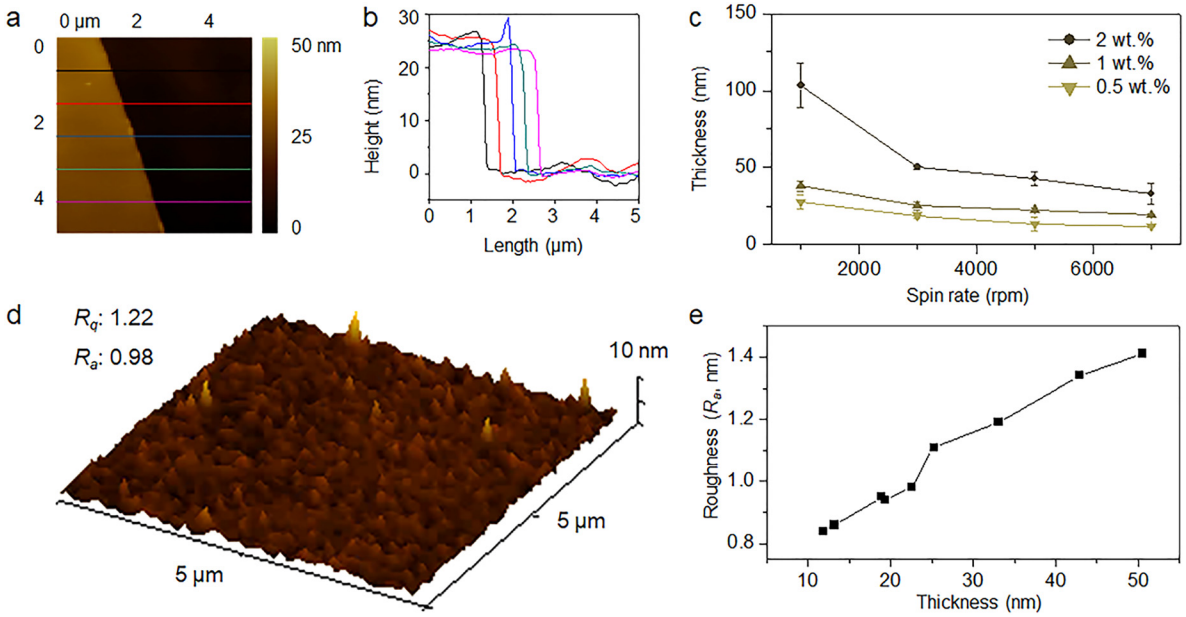

Fig. 2 Structural and morphological characterization of spin-coated silk fibroin thin films. (a) AFM image of the edge of a silk fibroin film prepared on a Si/SiO_2 substrate using a 1.0 wt% solution at 5000 rpm. (b) Height profiles taken across the film edge. (c) Dependence of silk fibroin film thickness on solution concentration, and spin-coating speed. (d) 3D AFM topography of a silk fibroin thin film (1.0 wt%, 5000 rpm). (e) Surface roughness of silk fibroin thin films as a function of film thickness.

both a surface profiler and AFM, as presented in Fig. 2, Fig. S2 and Table 1. Although minor discrepancies were observed between the two measurement methods, both consistently confirmed the same thickness trends as a function of concentration and spin speed.

As expected for polymer-derived thin films, the SF film thickness decreased systematically with decreasing solution concentration and increasing spin rate, ranging from 103.5 nm at 1000 rpm (2.0 wt%) to 8.9 nm at 7000 rpm (0.5 wt%). Films cast at 1000 rpm occasionally retained residual moisture during spinning, leading to local swelling and slight nonuniformity. Excluding these low-speed cases, the dependence of film thickness on concentration and spin rate followed a nearly linear trend, which is characteristic of centrifugal thinning dominated by polymer chain entanglement, solvent viscosity, and evaporation dynamics.[36,37]

The surface morphology of the spin-coated SF films was further examined by 3D AFM topography (Fig. S3). The AFM analysis showed that the surface roughness (R_a) decreased monotonically with decreasing SF concentration and increasing spin rate. Films prepared under higher dilution and faster spinning conditions exhibited smoother and more uniform surfaces, while those produced at lower spin speeds displayed slightly elevated roughness due to incomplete solvent removal and slower film consolidation. Although nanometer-scale island-like features were occasionally observed,[35] all SF thin films exhibited continuous, defect-free surfaces with low R_a values ranging from 0.84 to 1.41 nm. Moreover, R_a decreased

Table 1 Thickness of silk fibroin thin films prepared by spin coating with different spin rate and silk fibroin concentration measured by surface profiler and AFM

Spin rate (rpm)	Silk concentration					
	0.5 wt%		1 wt%		2 wt%	
	Surface profiler (nm)	AFM (nm)	Surface profiler (nm)	AFM (nm)	Surface profiler (nm)	AFM (nm)
1000	27.9 ± 4.5	—	38.2 ± 3.4	—	103.5 ± 14.1	—
3000	18.9 ± 2	19.1 ± 0.5	25.2 ± 2.8	24.9 ± 0.2	50.5 ± 1.7	50.3 ± 1.8
5000	13.1 ± 4.5	11.2 ± 0.4	22.6 ± 1.5	23.2 ± 0.7	42.9 ± 4.4	41.7 ± 1.6
7000	11.8 ± 1.1	8.9 ± 0.5	19.3 ± 1.1	19.9 ± 0.4	33.1 ± 6.9	37.8 ± 1.2

linearly with decreasing film thickness (Fig. 2e), demonstrating that the spin-casting parameters can be precisely tuned to produce highly smooth SF films, including sub-10-nm ultrathin layers suitable for uniform carbonization.

Microstructure development of SF-derived CNSs at different HTT

Before the pyrolysis process, the SF thin films were treated with methanol vapor to induce the formation of a β-sheet-rich structure that provide structural stability and serves as effective precursors for subsequent carbonization.[32,38] To establish the chemical baseline of the precursor, the XPS characteristics of regenerated SF were examined. Regenerated SF exhibits the typical elemental composition of protein-based materials, with carbon, oxygen, and nitrogen atomic fractions of 64, 21, and 15%, respectively (Table S1). These values are consistent with the amino-acid-derived theoretical composition of silk fibroin and confirm that the regenerated films retain the intrinsic chemical features of native SF.[39,40] This is further supported by the survey spectrum and deconvoluted high-resolution C1s and N1s spectra (Fig. S4), which reveal dominant C–C/C–H, C–N, O═C–N, and amide-related bonding environments characteristic of silk fibroin. Collectively, these results verify that the regenerated and methanol-treated SF films provide a chemically well-defined and structurally preserved starting material for high-temperature treatment.

The methanol-treated films were subsequently pyrolyzed at three different HTTs (800, 1000, and 1200 °C). During carbonization, the molecular chains of silk fibroin gradually transform from an amorphous organic state into a pseudo-graphitic carbon structure through a sequence of thermochemical reactions. To elucidate these changes, XPS, Raman, XRD, and FE-TEM analyses were conducted to investigate the chemical composition and structural evolution of SF-derived CNSs as a function of HTT. XPS analysis (Fig. 3 and Tables 2, 3) provides clear evidence of temperature-dependent heteroatom removal and carbon structural reorganization. Due to their proteinaceous nature, SF-based carbon materials exhibit high nitrogen and oxygen contents after carbonization by 800 °C. However, with increasing HTT, fraction from 80.98 to 92.07 at% and a

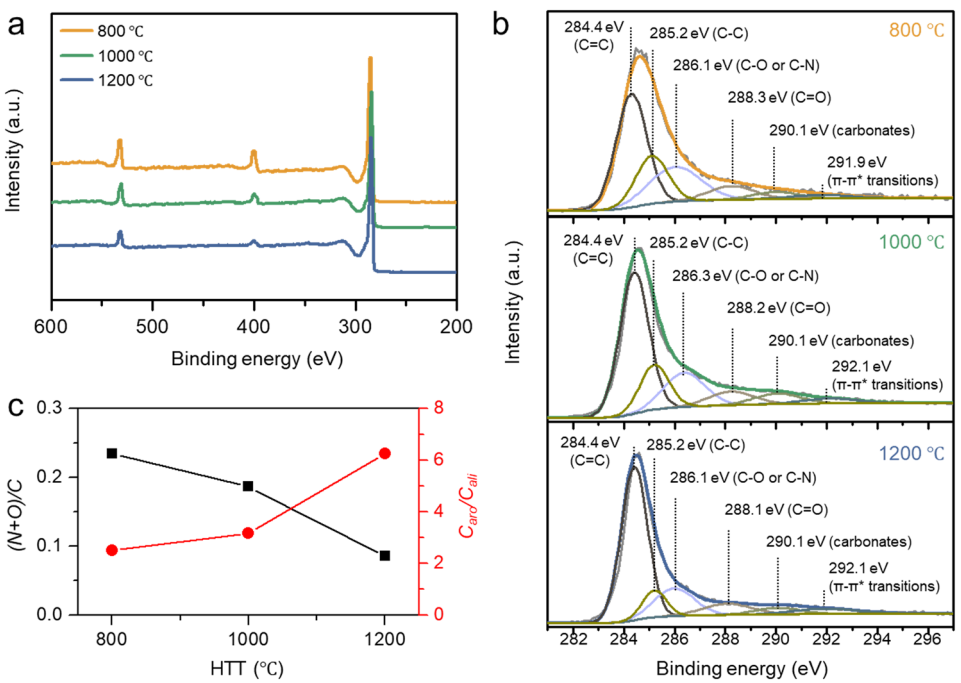

Fig. 3 (a) XPS survey spectra of silk-derived CNS and (b) their deconvolved C1s spectra carbonized at different temperatures. (c) The heteroatom-to-carbon ratio and the aromatic carbon-to-aliphatic carbon ratio derived from XPS analysis as a function of highest heat treatment temperature (HTT).

Table 2 Atomic content and atomic ratio of silk-derived CNS prepared by HTT of 800, 1000, and 1200 °C

	Atomic composition (at%)			Atomic ratio	
HTT (°C)	C1s	N1s	O1s	N/C	O/C
800	80.98	9.94	9.08	0.123	0.112
1000	84.25	7.66	8.09	0.091	0.096
1200	92.07	2.87	5.09	0.031	0.055

Table 3 Chemical composition of the silk-derived CNS obtained from C1s deconvolution results

	Composition (% of total carbon)					
HTT (°C)	Aromatic C=C	Aliphatic C–C	C–O/C–N	C=O	Carbonates	π–π*
800	46.29	18.51	19.79	7.69	4.99	2.73
1000	50.49	15.93	17.07	7.45	5.88	3.17
1200	58.23	9.32	15.81	7.37	4.53	4.73

corresponding decrease in nitrogen and oxygen contents from 9.94 to 2.87 at% and from 9.08 to 5.09 at%, respectively. This behavior is attributed to the progressive heteroatom elimination or conversion of the heteroatom-containing functional groups in carbon materials into stable, high-temperature resistant species during the high-temperature pyrolysis.[41,42] A significant decrease in heteroatom content (both nitrogen and oxygen) was observed between 1000 and 1200 °C (Fig. 3a), suggesting that major conversion steps occur within this higher temperature window. In parallel, spectral deconvolution of XPS C1s region (281–297 eV) of the heat-treated samples at 800, 1000, and 1200 °C (Fig. 3b) was performed using six peaks; 284.4, 282.2, 286.2, 288.2, 290.1 and 291.9 eV corresponding to C=C (aromatic carbon, C_{aro}), C–C (aliphatic carbon, C_{ali}), C–O/C–N, C=O, carbonates, and π–π* transition, respectively.[38,42,43] The integrated areas of the C1s peak components were calculated and summarized in Table 3. With increasing HTT from 800 to 1200 °C, the components of heteroatom-containing functional group (C–O/C–N, C=O, and carbonates) decreased from 19.79, 7.69, and 4.99% to 15.81, 7.37, and 4.53%, respectively. Concurrently, C_{ali} content decreased from 18.51 to 9.33%, while C_{aro} and π–π* transition contents increased from 46.29 and 2.73% to 58.23 and 4.73%, respectively. The C_{aro}/C_{ali} ratio and heteroatom-to-carbon ratio, (N + O)/C, were dramatically changed, when the HTT was increased from 1000 to 1200 °C as shown in Fig. 3c, reflecting that the carbon cluster consisting of sp^2 carbon atoms become dominant *via* heteroatom elimination and carbon re-organization reactions.[42–44] Moreover, the significant increase in π–π* by more than 70% between 1000 and 1200 °C confirms the increase of graphitic sp^2-hybridized carbon. These chemical and structural transformations are mirrored by macroscopic surface-property changes. The contact angle of a single water droplet on the surface of the SF-derived CNSs increased from 69.6 ± 0.4° (800 °C) and 70.9 ± 0.9° (1000 °C) to 75.1 ± 0.1° (1200 °C), reflecting the loss of polar heteroatom-containing functional groups and the emergence of a more hydrophobic, graphitic carbon surface (Fig. S5).

The structural evolution of SF-derived CNSs with increasing HTT was examined by XRD analysis (Fig. 4a). Regenerated silk fibroin exhibits characteristic Bragg reflections at approximately 9.6°, 19.8°, and 24.2°, corresponding to the (100), (210), and (002) planes of the β-sheet crystallites, respectively, which represent the typical β-sheet-rich crystalline structure of silk fibroin.[32] Upon carbonization, these β-sheet-related reflections disappeared completely, confirming the breakdown of the protein secondary structure and the formation of an amorphous carbon matrix. Instead, a broad diffraction feature centered near the (002) reflection of turbostratic carbon emerges

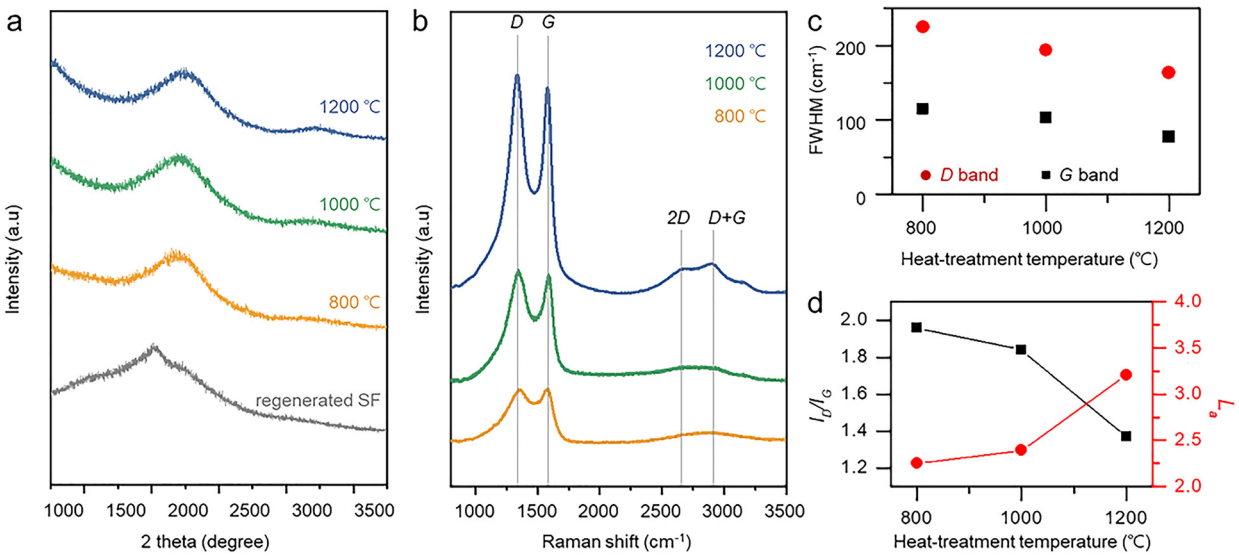

Fig. 4 (a) XRD patterns and (b) Raman spectra of silk-derived carbon nanosheets (CNSs) obtained at different heat treatment temperatures (HTTs). (c) Full width at half maximum (FWHM) of the D and G bands, and (d) the integral area ratio of the D to G bands (I_D/I_G) together with the in-plane crystallite size (L_a) as a function of HTT from 800 to 1200 °C.

for all carbonized samples. The (002) peak position shifts from 23.4° at 800 °C to 23.7° at 1000 °C and further to 24.8° at 1200 °C, accompanied by a concurrent narrowing of the peak. This systematic peak shift signifies a continuous reduction in the interlayer spacing (d_{002}), while the sharpening indicates an enhancement in local graphitic stacking. Such changes are well documented for carbon materials undergoing ordering transitions during high-temperature annealing, where heteroatom removal and layer reorganization lead to the formation of more compact sp^2-bonded carbon sheets. Microstructural development of SF-derived CNSs according to different HTT was further examined using Raman spectroscopy (Fig. 4b). For all the samples, two representative carbon bands, A_{1g} breathing mode of the sp^2 bonded carbon near the basal edge corresponding to structural defects (known as the D band) and the E_{2g} vibration mode of graphitic layers with sp^2 carbon (termed the *G* band) were detected at a frequency of around 1360 and 1580 cm^{-1}, respectively.[45,46] In particular, Raman spectrum of SF-based CNSs at HTT of 1200 °C showed a *2*D band at around 2675 cm^{-1} and a D + G band at around 2920 cm^{-1}, indicating the formation of graphitic stacked structure in CNSs, while the Raman spectra for SF-based CNSs at HTT of 800 °C and 1000 °C presented non-distinguishable weak and broad peaks in this region, reflecting less ordered carbon structure of CNSs. The first-ordered Raman region extending from 800 to 2000 cm^{-1} was deconvolved using four peaks as revealed in Fig. S6; D band, G bands, D″ band (amorphous sp^2 carbons) centered at around 1350 cm^{-1}, and I band (residual sp^3 carbons) centered at around 1100 cm^{-1}.[47,48] The peak position and width of the D and G bands can be used as indicators of the degree of graphitization.[49] The full width at half maximum (FWHM) and the peak position of D and G bands of SF-derived CNSs are plotted as a function of HTT in Fig. 4c and Fig. S7, respectively.

The FWHM of both D and G bands of CNSs was decreased from 224 and 115 to 163 and 77 cm^{-1}, respectively, with increasing HTT.

Namely, D and G bands became narrower and sharper as a result of the increasing of sp^2 carbon cluster portion in the CNSs. The shift of the G peak position toward the theoretical value for graphite (~1580 cm^{-1}) was observed while there were no obvious changes of the D band position (~1361 cm^{-1}). This evolution is consistent with that of the I_D/I_G ratio of the CNSs, which decreases from 1.96 at 800 °C to 1.37 at 1200 °C (Fig. 4d). The crystallite dimensions of the carbon layers (L_a) was calculated from the ratio of integral intensities of the D and G bands by using Tuinstra and Koenig equation as following;[50]

$$\frac{I_D}{I_G} = \frac{C(\lambda)}{L_a}$$

where $C(\lambda)$ is a constant, which depends on the laser wavelength ($C(\lambda)$ = 4.4 nm for the 514 nm laser used here). The L_a value was increased from 2.25 nm at 800 °C to 3.21 nm at 1200 °C. In particular, between 1000 and 1200 °C, it was confirmed that the formation of graphitic layer was accelerated, which is consistent with XPS results.

The microstructure of SF-based CNS films was further characterized by FE-TEM analysis, as shown in Fig. 5. Consistent with the XPS. XRD, and Raman results, the FE-TEM images reveal a clear temperature-dependent transition from amorphous to ordered carbon structures. At 800 °C, the CNSs exhibited an amorphous structure with small, poorly organized sp^2 carbon clusters. As the HTT reaches 1000 °C, short-range ordering becomes apparent, characterized by the emergence of turbostratic domains and partially aligned carbon layers. This structural evolution becomes even more pronounced at 1200 °C, where more distinct and densely packed graphitic features are observed. The corresponding SAED patterns further support these observations: diffuse halos at 800 °C develop into sharper diffraction rings at 1200 °C, particularly the (002) and (100) reflections of graphitic carbon. The increased definition of these rings confirms the progressive enhancement of interlayer coherence and in-plane hexagonal ordering with increasing HTT.

Morphological properties of SF-derived CNSs

The surface roughness and thickness of SF-derived CNS films prepared with various SF concentrations and HTTs were examined by AFM analysis (Fig. 6 and Fig. S8, S9). Although the surface roughness values increased slightly with increasing the SF concentration (from 0.5 to 2.0 wt%) and decreasing HTT

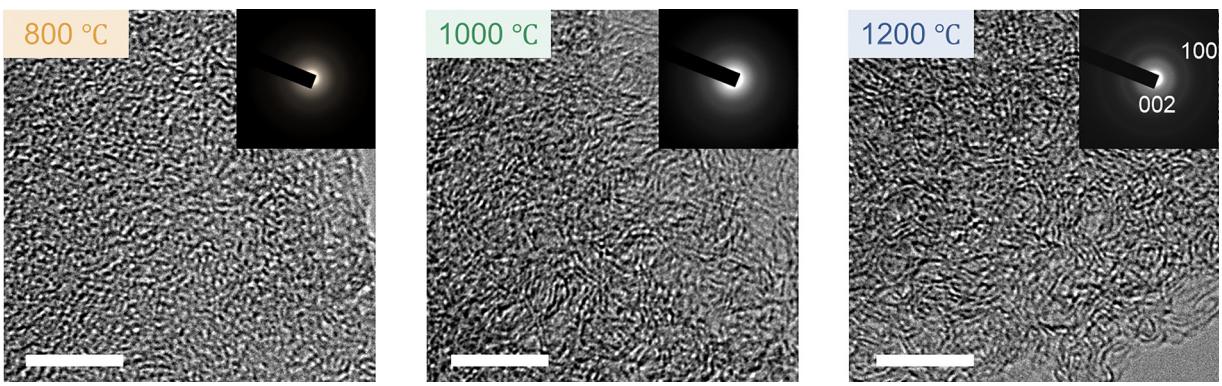

Fig. 5 FE-TEM and selected area diffraction patterns of the silk-derived carbon as a function of the highest heat treatment temperature (HTT). The scale bars represent 5 nm.

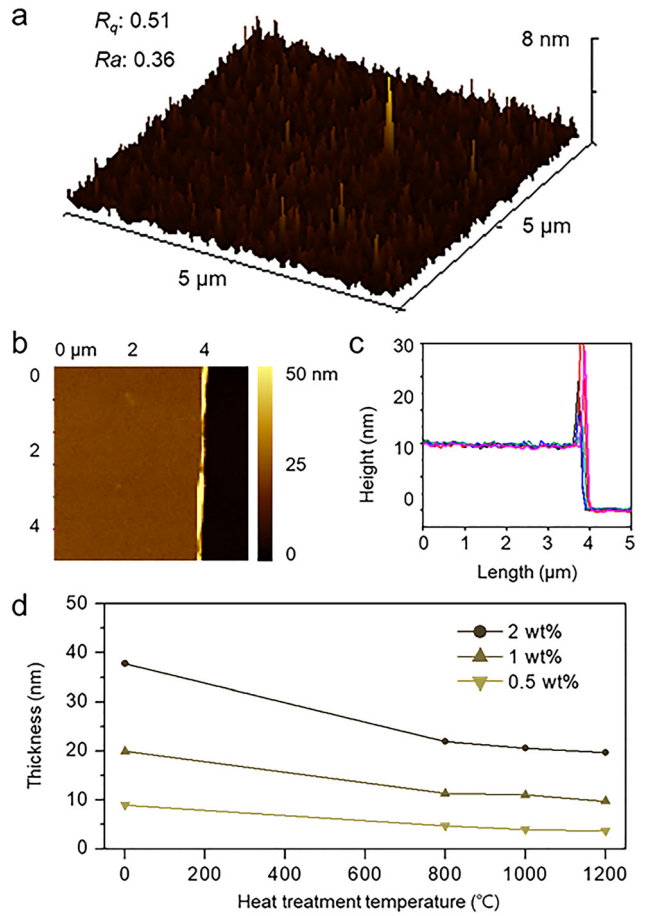

Fig. 6 (a) 3D AFM topography image of silk-derived CNS film after pyrolysis at 1200 °C using silk fibroin film prepared by 1 wt% solution and 7000 rpm. (b) AFM image of film edge and (c) their height profile across the film edge. (d) Thickness dependence of the silk fibroin-based carbon nanosheet film on the concentration of silk fibroin and the HTT (spin rate was 7000 rpm).

(a range from 800 to 1200 °C), it was confirmed that the CNS films prepared in this work displayed quite low R_a values within a range from 0.28 to 0.62 nm over the area of 5 × 5 μm^2, which is lower than those of previously reported CNS films using organic precursors as well as other types of TCFs fabricated using metal nanowires, carbon nanotubes, and graphene.[3,24,51–54] The low level of R_a values are evidence for relatively uniform and smooth TCF surfaces, which can reduce the possibility of leakage current and shorts.[54] As seen in Fig. 6d, the thickness of CNS films measured by AFM of film edge region decreased gradually with increasing HTT. Overall, the thickness values of CNS films derived from 0.5–2.0 wt% SF solutions ranged from 3.7 to 38.8 nm. Regardless of the initial thickness, the film thickness showed similar decrease ratio according to increasing HTT. After rapid decrease in thickness of about 50% due to the decomposition of protein molecules and chemical reactions forming carbon basic structural units at a relatively low temperature below 400 °C,[32] the thickness of CNS films were slightly decreased according to increasing HTT, concomitant with a decrease in heteroatom content shown in Fig. 3c.

Optical and electrical properties of SF-derived CNSs

The optical and electrical characteristics of the SF-derived CNSs were investigated after transferring the films onto commercial transparent PET substrates. As shown in Fig. 7, the transparency of the films was primarily determined by their nanoscale morphology. AFM analysis revealed thicknesses ranging from 3.7 to 38.8 nm with low surface roughness values (R_a = 0.28–0.62 nm), and these parameters exhibited a clear correlation with the measured transmittance. Namely, the transparency of the CNS films can be effectively tuned by adjusting the SF concentration and HTT, which controlled the final film thickness. As the thickness increased from 3.9 nm to 21.9 nm, the transmittance at 550 nm decreased from 95.7% to 70.4%, consistent with the well-known trade-off between optical transparency and electrical conductivity in TCFs. Notably, all CNS films prepared from a 0.5 wt% SF solution retained transmittance values higher than 90% at 550 nm, indicating minimal optical scattering even after high-temperature carbonization.[55]

The electrical transport properties of the CNS films were evaluated using the standard four-point probe method. As shown in Fig. 8a, the sheet resistance (R_{sheet}) decreased with increasing HTT. This behavior can be attributed to enhanced graphitic ordering and the removal of heteroatom-containing species, as confirmed by XPS, Raman spectroscopy, FE-TEM and diffraction analyses. Moreover, R_{sheet} also decreased with increasing film thickness, likely due to reduced surface roughness and improved charge-carrier pathways, as evidenced by AFM analysis (Fig. S8). The electrical conductivity values for various CNS films were calculated using the following equation;

$$\sigma = \frac{1}{(R_{sheet} \times t)}$$

where, σ is the electrical conductivity, t is the film thickness, and R_{sheet} is the value of sheet resistance. As displayed in Fig. 8b, the conductivity of SF-derived CNS films increased with

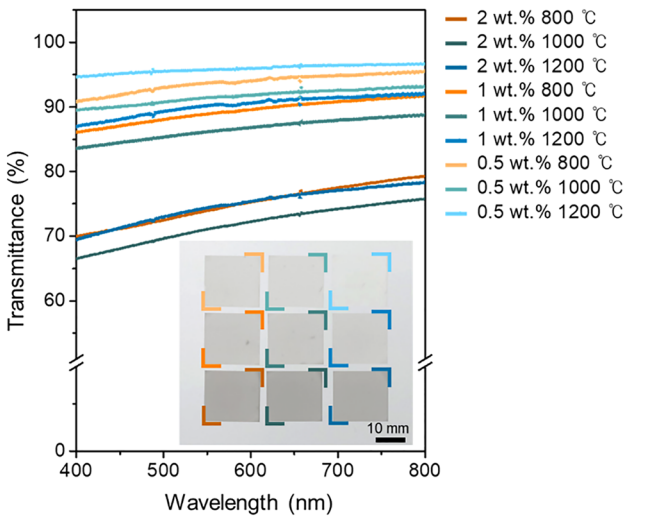

Fig. 7 Transmittances of silk-derived CNS films obtained with different SF concentrations and HTTs after transferring on to PET. (Inset) optical image of all silk-derived CNS films.

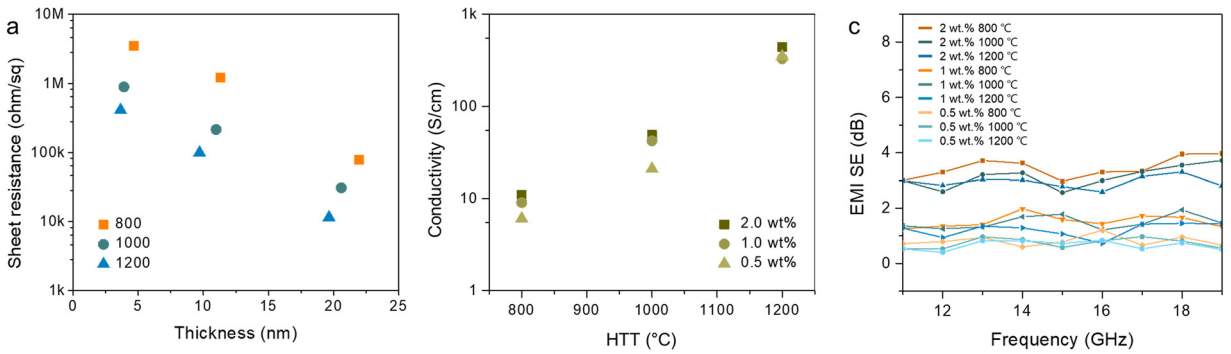

Fig. 8 (a) Sheet resistance of silk-derived CNS film prepared with different HTT as a function of film thickness. (b) Electrical conductivity of the CNS films with different concentration as a function of HTT. (c) EMI SE of silk fibroin-derived TCF as a function of frequency measured in the 9–19 GHz range.

HTT, which is consistent with the structural evolution observed in XPS and Raman spectra. Increasing HTT resulted in higher aromatic carbon content, reduced heteroatom concentration, and a lower I_D/I_G ratio accompanied by larger crystallite sizes, indicating the formation of more continuous sp^2-bonded carbon networks.[56,57] TEM images further supported this observation by showing the emergence of graphitic stacking at higher HTTs. Variations in SF concentration (0.5–2.0 wt%) produced minimal differences in conductivity at a fixed HTT, demonstrating that the initial film thickness has a limited effect when the microstructure is comparable. Taken together, these results indicate that both the microstructural development driven by high-temperature graphitization and the morphological factors controlled through the initial film deposition play important roles in determining the optical and electrical performance of the CNS films. Films carbonized at 1200 °C achieved an average conductivity of approximately 3.5×10^2 S cm^{-1}, surpassing that of TCFs prepared from other polymer-derived CNSs as well as chemically exfoliated or reduced graphene materials.[26,51]

Electromagnetic interference (EMI) shielding performance of the SF-derived CNS TCFs was also examined in the 9–19 GHz frequency range (Fig. 8c). The EMI shielding effectiveness (SE) exhibited a positive correlation with both HTT and film thickness. Although the SE values of the present CNS films remain moderate for commercial applications, the thicker films fabricated from higher SF concentrations achieved noticeably enhanced SE, reflecting the intrinsic improvement in electrical conductivity and EMI shielding efficiency with increasing graphitization and enhanced sp^2 domain connectivity.[46] Collectively, these results demonstrate that SF-derived CNS films offer a tunable balance between optical transparency, electrical conductivity, and EMI shielding performance. The combination of high transparency (>90%), moderate sheet resistance, and the sustainable bio-derived origin underscores their potential as promising candidates for next-generation flexible transparent electrodes in wearable and optoelectronic systems. In comparison with other categories of carbon-based transparent conductive films (TCFs), graphene and carbon-nanotube (CNT) networks provide the highest electrical performance but typically require high-temperature CVD growth, delicate transfer steps, and chemical doping, which limit their scalability and compatibility with flexible substrates. Polymer-derived carbon nanosheets (CNSs), including the silk-derived CNSs in this study, can instead be produced *via* simple solution processing and thermal conversion without catalysts or corrosive reagents. Although the sheet resistance of the silk-CNS electrodes is higher than that of graphene or CNT networks, the values achieved here (>98% transmittance at $\sim 10^2$ Ω sq^{-1}) are comparable to, or in some cases better than, those reported for other polymer-based CNS systems such as polyimide-, polyethylene-, and PAN-derived films. As summarized in Supplementary Table S2, silk-derived CNSs thus occupy a distinct position among solution-processed carbon electrodes, offering exceptionally high transparency, moderate conductivity, strong mechanical robustness, and a fully bio-sourced precursor. Beyond these performance metrics, this study advances the broader understanding of silk-derived carbon nanosheets. While previous work on polymer-derived CNSs has primarily explored micrometer-thick or opaque structures for energy storage or structural applications, the present study establishes an alternative materials platform based on ultrathin, sub-10-nm SF-derived CNS films with high transparency, smooth morphology, and electrical conductivity. Our systematic analysis further shows that the precursor film thickness and the heat-treatment temperature work together to control the nanoscale microstructure and the resulting optoelectronic properties. This integrated processing–structure–property insight has not been previously reported for silk-based carbon materials and provides an important foundation for the rational design of bio-derived CNS films for transparent electrode applications.

Conclusion

In this work, we demonstrated a simple approach for fabricating transparent conductive films based on ultrathin silk-derived CNSs. Spin-coated SF precursor films with tunable thicknesses (10–100 nm) were converted into conductive CNS layers through controlled pyrolysis, and structural analyses confirmed the gradual development of graphitic domains with increasing HTT. The resulting CNS films exhibited high optical

transparency (up to 95.7% at 550 nm) and electrical conductivity (4.4×10^2 S cm^{-1}), indicating performance comparable to other solution-processed nanocarbon electrodes. These results highlight the potential of silk fibroin as a renewable and solution-processable precursor for flexible transparent electrodes. Although the present study demonstrates the feasibility of silk-derived CNS TCFs with excellent transparency and moderate conductivity, several limitations remain. The electrical performance, while competitive with other solution-processed carbon electrodes, is still lower than that of high-quality CVD graphene, suggesting that further optimization of graphitic ordering or heteroatom control may be beneficial. In addition, the current spin-coating approach produces uniform films on small substrates; future efforts toward scalable roll-to-roll processing, improved mechanical durability under repeated bending, and integration with device architectures will be important steps toward practical applications. Finally, understanding the long-term environmental stability and interaction with encapsulation layers will further advance the use of silk-derived CNS films in flexible optoelectronics.

Conflicts of interest

There are no conflicts to declare.

Data availability

The data supporting this article have been included as part of the supplementary information (SI). Supplementary information provides additional experimental details and supporting characterization data. This includes the temperature profile used for silk fibroin carbonization (Fig. S1); AFM thickness measurements of spin-cast silk fibroin precursor films as a function of solution concentration and spin speed (Fig. S2); 3D AFM topography images and corresponding surface roughness analyses of precursor silk films (Fig. S3); XPS survey and high-resolution C1s and N1s spectra of regenerated silk fibroin (Fig. S4); water contact angle measurements of silk-derived carbon nanosheets prepared at different heat-treatment temperatures (Fig. S5); deconvoluted Raman spectra and evolution of D and G band positions with heat-treatment temperature (Fig. S6 and S7); AFM surface roughness and thickness measurements of carbonized silk fibroin nanosheet films prepared under various processing conditions (Fig. S8 and S9); elemental composition analysis of regenerated silk fibroin (Table S1); and a comparative table summarizing representative carbon-based transparent conductive films reported in the literature (Table S2). These supplementary data provide further insight into the structure–property relationships and reproducibility of the silk-derived carbon nanosheets discussed in the main text. See DOI: https://doi.org/10.1039/d5tc03917g.

Acknowledgements

This research was supported by the National Science Foundation (NSF) under CAREER award number 2239244 (any opinions, findings, and conclusions or recommendations expressed in this material are those of the author(s) and do not necessarily reflect the views of the National Science Foundation). Work was also supported by the Department of Mechanical Engineering and Materials Science at the University of Pittsburgh. Fabrication and characterization was performed, in part, at the Nanoscale Fabrication and Characterization Facility, a laboratory of the Gertrude E. and John M. Petersen Institute of NanoScience and Engineering, housed at the University of Pittsburgh, and in part, at Materials Characterization Laboratory, housed at Department of Chemistry in the University of Pittsburgh. This work was also partially supported by the National Research Council of Science & Technology (NST) grant by the Korea government (MSIT) (CRC23013-000).

References

1 Y. Wang, C. Zhu, R. Pfattner, H. Yan, L. Jin, S. Chen, F. Molina-Lopez, F. Lissel, J. Liu, N. I. Rabiah, Z. Chen, J. Won Chung, C. Linder, M. F. Toney, B. Murmann and Z. Bao, *Sci. Adv.*, 2017, **3**, 1602076.
2 J. Ning, L. Hao, M. Jin, X. Qiu, Y. Shen, J. Liang, X. Zhang, B. Wang, X. Li and L. Zhi, *Adv. Mater.*, 2017, **29**, 1–8.
3 J. Lee, K. An, P. Won, Y. Ka, H. Hwang, H. Moon, Y. Kwon, S. Hong, C. Kim, C. Lee and S. H. Ko, *Nanoscale*, 2017, **9**, 1978–1985.
4 S. Y. Son, Y. J. Noh, C. Bok, S. Lee, B. G. Kim, S. I. Na and H. I. Joh, *Nanoscale*, 2014, **6**, 678–682.
5 S. Jiang, P. X. Hou, M. L. Chen, B. W. Wang, D. M. Sun, D. M. Tang, Q. Jin, Q. X. Guo, D. D. Zhang, J. H. Du, K. P. Tai, J. Tan, E. I. Kauppinen, C. Liu and H. M. Cheng, *Sci. Adv.*, 2018, **4**, eaap9264.
6 C. Pavlou, M. G. Pastore Carbone, A. C. Manikas, G. Trakakis, C. Koral, G. Papari, A. Andreone and C. Galiotis, *Nat. Commun.*, 2021, **12**, 1–9.
7 D. A. Ilatovskii, E. P. Gilshtein, O. E. Glukhova and A. G. Nasibulin, *Adv. Sci.*, 2022, **9**, 1–16.
8 D. Won, J. Bang, S. H. Choi, K. R. Pyun, S. Jeong, Y. Lee and S. H. Ko, *Chem. Rev.*, 2023, **123**, 9982–10078.
9 M. Althumayri, R. Das, R. Banavath, L. Beker, A. M. Achim and H. Ceylan Koydemir, *Adv. Sci.*, 2024, **11**, 1–25.
10 M. R. Azani, A. Hassanpour and T. Torres, *Adv. Energy Mater.*, 2020, **10**, 1–32.
11 Y. Leterrier, L. Médico, F. Demarco, J. A. E. Månson, U. Betz, M. F. Escolà, M. K. Olsson and F. Atamny, *Thin Solid Films*, 2004, **460**, 156–166.
12 V. Zardetto, T. M. Brown, A. Reale and A. Di Carlo, *J. Polym. Sci., Part B: Polym. Phys.*, 2011, **49**, 638–648.
13 V. Nam and D. Lee, *Nanomaterials*, 2016, **6**, 47.
14 W. He and C. Ye, *J. Mater. Sci. Technol.*, 2015, **31**, 581–588.
15 B. J. Worfolk, S. C. Andrews, S. Park, J. Reinspach, N. Liu, M. F. Toney, S. C. B. Mannsfeld and Z. Bao, *Proc. Natl. Acad. Sci. U.S.A.*, 2015, **112**, 14138–14143.

16 Q. Zheng, Z. Li, J. Yang and J. K. Kim, *Prog. Mater. Sci.*, 2014, **64**, 200–247.
17 S. Bae, H. Kim, Y. Lee, X. Xu, J. S. Park, Y. Zheng, J. Balakrishnan, T. Lei, H. Ri Kim, Y. Il Song, Y. J. Kim, K. S. Kim, B. Özyilmaz, J. H. Ahn, B. H. Hong and S. Iijima, *Nat. Nanotechnol.*, 2010, **5**, 574–578.
18 J. J. Patil, W. H. Chae, A. Trebach, K. J. Carter, E. Lee, T. Sannicolo and J. C. Grossman, *Adv. Mater.*, 2021, **33**, 1–29.
19 J. Wan, Y. Chen, W. Chen, J. Xia, G. Zeng, J. Cao, C. Jin, Y. Shen, X. Wu, H. Chen, J. Ding, X. M. Ou, Y. Li and Y. Li, *Sci. China: Chem.*, 2024, **67**, 3347–3356.
20 Y. Zhu, S. Murali, W. Cai, X. Li, J. W. Suk, J. R. Potts and R. S. Ruoff, *Adv. Mater.*, 2010, **22**, 3906–3924.
21 Y. L. Zhong, Z. Tian, G. P. Simon and D. Li, *Mater. Today*, 2015, **18**, 73–78.
22 Y. Si and E. Samulski, *Nano Lett.*, 2008, **8**, 1679–1682.
23 Y. Song, W. Fang, R. Brenes and J. Kong, *Nano Today*, 2015, **10**, 681–700.
24 R. Li, K. Parvez, F. Hinkel, X. Feng and K. Müllen, *Angew. Chem., Int. Ed.*, 2013, **52**, 5535–5538.
25 D. Choi, J.-S. Yeo, H.-I. Joh and S. Lee, *ACS Sustainable Chem. Eng.*, 2018, **6**, 8b03066.
26 H. Souri, S. J. Yu, H. Yeo, M. Goh, J. Y. Hwang, S. M. Kim, B. C. Ku, Y. G. Jeong and N. H. You, *RSC Adv.*, 2016, **6**, 52509–52517.
27 G. N. Tomaraei, S. Y. Cho, M. Abdulhafez and M. Bedewy, in *Biomaterial and Prototyping Application in Medicine*, ed. P. Bartolo and B. Bidanda, Springer, 2020.
28 J. K. Sahoo, O. Hasturk, T. Falcucci and D. L. Kaplan, *Nat. Rev. Chem.*, 2023, **7**, 302–318.
29 Y. Zhu, W. Sun, J. Luo, W. Chen, T. Cao, L. Zheng, J. Dong, J. Zhang, M. Zhang, Y. Han, C. Chen, Q. Peng, D. Wang and Y. Li, *Nat. Commun.*, 2018, **9**, 3861.
30 Y. S. Yun, S. Y. Cho, H. Kim, H. J. Jin and K. Kang, *ChemElectroChem*, 2015, **2**, 359–365.
31 Y. S. Yun, S. Y. Cho, J. Shim, B. H. Kim, S. J. Chang, S. J. Baek, Y. S. Huh, Y. Tak, Y. W. Park, S. Park and H. J. Jin, *Adv. Mater.*, 2013, **25**, 1993–1998.
32 S. Y. Cho, Y. S. Yun, S. Lee, D. Jang, K. Y. Park, J. K. Kim, B. H. Kim, K. Kang, D. L. Kaplan and H. J. Jin, *Nat. Commun.*, 2015, **6**, 1–7.
33 D. N. Rockwood, R. C. Preda, T. Yücel, X. Wang, M. L. Lovett and D. L. Kaplan, *Nat. Protoc.*, 2011, **6**, 1612–1631.
34 S. Y. Cho, M. Abdulhafez, M. E. Lee, H.-J. Jin and M. Bedewy, *ACS Appl. Nano Mater.*, 2018, **1**, 5441–5450.
35 C. Jiang, X. Wang, R. Gunawidjaja, Y. H. Lin, M. K. Gupta, D. L. Kaplan, R. R. Naik and V. V. Tsukruk, *Adv. Funct. Mater.*, 2007, **17**, 2229–2237.
36 M. H. Park, J. Kim, S. C. Lee, S. Y. Cho, N. R. Kim, B. Kang, E. Song, K. Cho, H.-J. Jin and W. H. Lee, *RSC Adv.*, 2016, **6**, 5907–5914.
37 D. B. Hall, P. Underhill and J. M. Torkelson, *Polym. Eng. Sci.*, 1998, **38**, 2039–2045.
38 S. Y. Cho, Y. S. Yun, D. Jang, J. W. Jeon, B. H. Kim, S. Lee and H. J. Jin, *Nat. Commun.*, 2017, **8**, 1–7.
39 H. J. Jin, S. V. Fridrikh, G. C. Rutledge and D. L. Kaplan, *Biomacromolecules*, 2002, **3**, 1233–1239.
40 J. Shao, J. Liu, J. Zheng and C. M. Carr, *Polym. Int.*, 2002, **51**, 1479–1483.
41 J. H. Zhou, Z. J. Sui, J. Zhu, P. Li, D. Chen, Y. C. Dai and W. K. Yuan, *Carbon*, 2007, **45**, 785–796.
42 R. J. J. Jansen and H. van Bekkum, *Carbon*, 1995, **33**, 1021–1027.
43 Y. I. S. I. Koei Nishimiya and T. Hata, *J. Wood Sci.*, 1998, **44**, 56–61.
44 V. Datsyuk, M. Kalyva, K. Papagelis, J. Parthenios, D. Tasis, A. Siokou, I. Kallitsis and C. Galiotis, *Carbon*, 2008, **46**, 833–840.
45 A. C. Ferrari and J. Robertson, *Phys. Rev. B:Condens. Matter Mater. Phys.*, 2001, **64**, 1–13.
46 A. C. Ferrari and J. Robertson, *Phys. Rev. B*, 2000, **61**, 95–107.
47 C. Hu, S. Sedghi, A. Silvestre-Albero, G. G. Andersson, A. Sharma, P. Pendleton, F. Rodríguez-Reinoso, K. Kaneko and M. J. Biggs, *Carbon*, 2015, **85**, 147–158.
48 Y. R. Rhim, D. Zhang, D. H. Fairbrother, K. A. Wepasnick, K. J. Livi, R. J. Bodnar and D. C. Nagle, *Carbon*, 2010, **48**, 1012–1024.
49 A. Cuesta, P. Dhamelincourt, J. Laureyns, A. Martínez-Alonso and J. M. D. Tascón, *Carbon*, 1994, **32**, 1523–1532.
50 F. Tuinstra and J. L. Koenig, *J. Chem. Phys.*, 1970, **53**, 1126–1130.
51 S. I. Na, Y. J. Noh, S. Y. Son, T. W. Kim, S. S. Kim, S. Lee and H. I. Joh, *Appl. Phys. Lett.*, 2013, **102**(4).
52 L. Yu, C. Shearer and J. Shapter, *Chem. Rev.*, 2016, **116**, 13413–13453.
53 T. Sannicolo, M. Lagrange, A. Cabos, C. Celle, J. P. Simonato and D. Bellet, *Small*, 2016, **12**, 6052–6075.
54 Z. C. Gomez De Arco, L. Zhang, Y. Schlenker, C. W. Ryu, K. Thompson ME, L. Gomez De Arco, Y. Zhang, C. W. Schlenker, K. Ryu, M. E. Thompson and C. Zhou, *ACS Nano*, 2010, **4**, 2865.
55 Z. J. Fan, J. Yan, T. Wei, G. Q. Ning, L. J. Zhi, J. C. Liu, D. X. Cao and F. Wei, *ACS Nano*, 2011, **5**, 2787–2794.
56 M. S. Dresselhaus, A. Jorio, M. Hofmann, G. Dresselhaus and R. Saito, *Nano Lett.*, 2010, **10**, 751–758.
57 A. C. Ferrari and D. M. Basko, *Nat. Nanotechnol.*, 2014, **8**, 235–246.